Plasma Chemistry and Plasma Processing (2023) 43:787–803
https://doi.org/10.1007/s11090-023-10328-9

ORIGINAL PAPER

Heat Transfer Mechanisms in Arcs of Various Gases at Atmospheric Pressure

Rodrigo Villarreal-Medina[1] · Anthony B. Murphy[2] · Patricio F. Méndez[3] · Marco A. Ramírez-Argáez[1]

Received: 17 November 2022 / Accepted: 29 March 2023 / Published online: 23 April 2023
© The Author(s) 2023

Abstract

This work expands findings about the dominant heat transfer mechanisms in argon and helium arcs at atmospheric pressure for monoatomic (Ar, He, 50% Ar–50% He), diatomic (air, N_2, O_2, F_2, Cl_2), and triatomic (CO_2) gases. The objective is to understand the dominant mechanisms in atmospheric plasmas through validated numerical modeling for GTAW welding process. Arcs of all gases have lengths of 10 mm and 200 A current. Five heat transfer mechanisms are considered: Joule heating, convection, radiation, conduction, and Thomson effect. Results indicate that the general structure of the arcs and dominant mechanisms are qualitatively similar for all gases; sizes change depending on the gas. The dominant energy input near the cathode is Joule heating, while that near the anode is convection. The dominant energy output always follows the same sequence: Thomson effect next to the cathode followed by convection, radiation in the arc column, and conduction near the anode. Joule heating is the most significant in Ar, while in He, it has the lowest significance. This is due to differences in electric conductivity of He (higher up to 21,000 K and lower beyond 21,000 K than other gases) and high viscosity of He, which creates a small Joule heating versus a large convection region. He transfers the most heat towards the anode by convection while N_2 has the lowest; due to the high enthalpy and viscosity of He compared to N_2. Finally, Ar has the most significant radiative emission and He the smallest due to their net emission coefficient.

Keywords Electric arc · GTAW · Heat transfer · Numerical modeling

✉ Marco A. Ramírez-Argáez
marco.ramirez@unam.mx

[1] Metallurgical Engineering Department, School of Chemistry, UNAM, Mexico City, Mexico

[2] CSIRO Manufacturing, PO Box 218, Lindfield, NSW 2070, Australia

[3] Department of Chemical and Materials Engineering, University of Alberta, Edmonton, Canada

Introduction

Arcs at atmospheric pressure are ubiquitous in modern technology, including arc welding, high-current switches, and electric arc furnaces. Arc welding in particular is used in applications as small as morphine pumps welded with 1 A, to aircraft carriers welded with currents approaching 1000 A, and gases involved range from pure Ar to molecular gases such as CO_2. When there are multiple options, the selection of gases is done exclusively empirically, based on past knowledge and trial and error. In some processes such as submerged arc welding, the arc gases come from the evaporation of ceramic fluxes and evaporating metals [1]. An understanding of arc behavior in general, extending beyond specific cases, will be much welcome by practitioners. In most technologies involving arcs at atmospheric pressure, heat transfer is the key consideration. In high-current switches, melting and thermal damage are to be avoided, while in welding and electric arc furnaces, the arcs are meant to melt metal (typically the anode). Heat transferred from the arc to the joint depends on arc length, input current, shielding gas, and electrode type, among other parameters [2–5].

Experimental studies of heat transfer in the arc are rarely found in the literature. Due to the emission of arc radiation, measuring thermal and electric characteristics of welding arcs is usually done by optical emission spectroscopy measurements. However, high-speed cameras with optical filters and laser illumination systems or thermocouple arrays can also be used [6–8]. The measurement of arc characteristics is a way to validate mathematical models of the arc, which have been the most widely used analysis tool.

The heat transfer from the arc to the workpiece is very commonly estimated by assuming that the arc is a moving heat source. The source can be either a point, a line, or a volumetric heat source. Also the heat distribution can be Gaussian [9], elliptic [10], double elliptic [11] or a combination of these [12, 13]. All these distributions have a central peak that decreases very rapidly along the workpiece domain. This approach allows estimation of characteristics such as the location of the heat affected zone and provides a way to compute residual stresses but neglects the physical phenomena inside the arc. Moreover, the heat source has to be calibrated against measurements, for example of the thermal history at locations in the workpiece.

Heat transfer inside the arc is a complex phenomenon that encompasses many mechanisms such as convection due to the plasma jet, heat conduction, and radiation from and within the arc [2, 14]. It is well established that the Joule effect and radiation are the main heat input and heat output in the arc plasma, respectively. Nonetheless, near the electrodes, the temperature difference between the electrons and other species present in the arc means that the local thermal equilibrium assumption is not valid, and mechanisms like Thomson effect, electron drift and electron absorption must be considered.

Based on the above, it cannot be denied that heat transfer phenomena inside the arc play a fundamental role in welding technology. The topic has been researched, but not to the extent that accords with its importance. For example, Lu et al. [15] identified the best-operating conditions in a GMAW process to maximize heat transfer between the arc and aluminum plates using a three-dimensional numerical model that includes the filler wire, arc plasma and a meltable workpiece. They found that 99% of the energy generated in the arc is due to Joule heating. Furthermore, the arc consumes 14–19% of the total energy, so the arc efficiency is 66–77% in this system.

Schnick et al. [16] conceptualized the arc columns as two concentric cylinders. The inner cylinder had argon and metal vapor present from the wire evaporation; meanwhile,

the outer cylinder was considered to be composed only of argon. In the inner cylinder, they found that even a small amount of metal vapor increases the radiation losses significantly and thus decreases the arc temperature. They also used a 2D axisymmetric CFD model to simulate GMAW welding and found that local radiation and resistive heating values have the same order of magnitude as convection and heat conduction. Thus, these components cannot be neglected in the global energy balance for MIG arcs.

Recently, maps of the dominant heat transfer mechanism were developed by Velazquez et al. [17], creating a simple way to present the main features of heat transfer in TIG welding using helium and argon as shielding gases. The maps were obtained by processing the results of numerical simulations and they provided the isotherms and isopleths of radiative emission of the arc, and the distribution of the dominant heat transfer mechanisms inside the arc and their relative importance in the form of color maps. They analyzed the changes in these maps that occurred when current input and arc length were varied. While the arc length modified the region the workpiece in which convection dominated, the arc current impacts the region and degree of dominance of all mechanisms, in particular the Joule effect. Also, they predicted that shielding gas would modify the region and degree of each mechanism's dominance. The details on the construction of such maps may be seen in [17].

The purpose of the work is not the development of model, which has been already developed and validated extensively in the literature. Instead, the numerical model is applied to assess quantitatively the relative importance of each of the heat transfer mechanisms in the arc column for nine different plasma gases, including monoatomic, diatomic, triatomic and a mixture. This constitutes the originality of the work.

Methodology

Mathematical Model

This work builds on the model of the arc at atmospheric pressure developed originally in [18], and used recently in [17, 19, 20]. The model considers the arc to be axisymmetric (Fig. 1), which is true for electric arc furnaces, high current switches, and a large number of welding applications such as GTAW. Because this model has been validated extensively in the literature, its key features will be described only briefly.

The main assumptions made in the model are listed in Table 1, which result in the governing equations listed in Table 2, with the boundary conditions listed in Table 3. The notation is given in "Appendix 2". It is worth mentioning that due to the LTE assumption, energy fluxes associated with the electron and ion drift and diffusion fluxes (apart from that connected with the electric current density) are not considered. Also, the inclusion of sheath voltages in the model could modify the properties of the arcs formed from the different gases.

Solution and Generation of the Maps

The model was cast in the CFD software PHOENICS version 2017, and numerically solved using an entirely orthogonal grid of 60×60 cells that was the output of a grid sensitivity analysis previously presented [18]. For the work, nine different simulations were performed keeping the same arc length of 10 mm and the arc current of 200 A; the type of gas is varied. The physical properties of the nine gases (air, helium, argon,

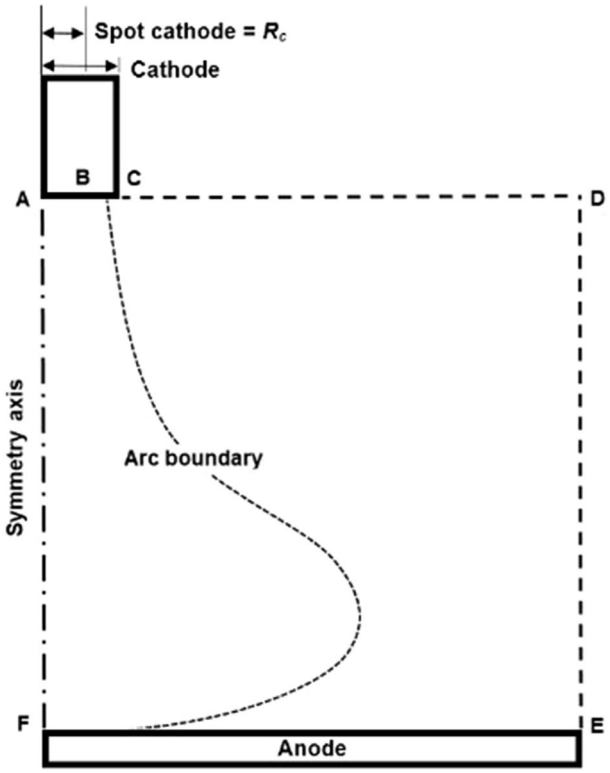

Fig. 1 Computational domain of the DC electric arc regions

50–50% He–Ar mixture, CO_2, O_2, N_2, F_2 and Cl_2) were computed using the methods presented by Murphy et al. [23–26]. "Appendix 1" provides details of the calculations made to obtain the physical properties of F_2 and Cl_2. Some plasma gases (air, O_2, F_2, Cl_2) are impractical for welding, particularly with a tungsten cathode, but are helpful to gain a theoretical understanding of the arc physics and particularly the heat transfer mechanisms as a function of the plasma properties. FORTRAN subroutines were written to compute the electromagnetic problem, the source terms of the momentum and energy conservation equations, as well as some boundary conditions. Several subroutines were created to calculate the five heat transfer mechanisms in Watts per cubic meter inside the arc (positive or negative terms). Then, as stated in our previous work [17], a subroutine in Matlab® was used to construct the map of the dominant heat transfer mechanisms, showing the intensity of the largest heat transfer mechanism in each cell for both inputs and outputs of energy. Also, the shape of the arc, defined by the isotherm at which the conductivity approaches zero (the external isotherm) is drawn, and the relative importance of the dominant mechanisms to the rest of the mechanisms is shown through isolines. Every run took around 50,000 iterations and approximately 2 h of computation time to provide a converged solution (when the conservation equation's imbalances reached a level below 0.001%) on an Intel® Xeon® CPU E31245 3.30 GHz computer. The model was extensively validated by comparing the predicted results against other simulations and experimental data of most of the arc characteristics and arc-weld pool interactions, as can be seen in previous published works [18, 27].

Table 1 List of simplifying assumptions used in the development of the mathematical model

Assumption	Consequence
Plasma is in local thermodynamic equilibrium (LTE)	All species in the plasma have the same temperature, which is valid for a high-pressure discharge and allows us to compute a one-temperature arc column
2D axisymmetric domain	The use of axisymmetric 2D cylindrical polar coordinates
Steady-state	The time derivatives are zero since it is a DC system
Non-slip and impermeable anode and cathode surfaces	All components of the velocity vector are zero at the condensed boundaries
Flat anode surface	The plasma jet impinging the weld pool does not deform the free surface
Only the plasma gas is present	Metal vapors are not considered; this is generally reasonable for TIG arcs
Laminar flow regime	According to an order of magnitude determination, the Reynolds number is below the transition from laminar to turbulent regime for free jets
Electromagnetic convection is neglected	The magnetic Reynolds number computed for this arcs show the correctness of using this assumption. Ohm's law has only the diffusive term
Anode and cathode fall regions are not explicitly solved in this model	We used a discretized domain such that the mesh near the electrodes contains the anode and cathode fall regions
Cathode temperature is 3493 K	We neglect any possible effect of the change of shielding gas on cathode temperature

Table 2 Governing equations

Name	Equation
Continuity	$\frac{\partial}{\partial z}\left(\rho v_z\right)+\frac{1}{r}\frac{\partial}{\partial r}\left(\rho r v_r\right)=0$
Navier–Stokes—z	$\frac{\partial}{\partial z}\left(\rho v_z^2\right)+\frac{1}{r}\frac{\partial}{\partial r}\left(\rho r v_r v_z\right)=-\frac{\partial P}{\partial z}+2\frac{\partial}{\partial z}\left(\mu\frac{\partial v_z}{\partial z}\right)+\frac{1}{r}\frac{\partial}{\partial r}\left(r\mu\left[\frac{\partial v_z}{\partial r}+\frac{\partial v_r}{\partial z}\right]\right)-B_\theta J_r$
Navier–Stokes—r	$\frac{1}{r}\frac{\partial}{\partial r}\left(\rho r v_r^2\right)+\frac{\partial}{\partial z}\left(\rho v_r v_z\right)=-\frac{\partial P}{\partial r}+\frac{\partial}{\partial z}\left(\mu\left[\frac{\partial v_z}{\partial r}+\frac{\partial v_r}{\partial z}\right]\right)+\frac{2}{r}\frac{\partial}{\partial r}\left(r\mu\frac{\partial v_r}{\partial z}\right)-\frac{2\mu v_r}{r^2}+B_\theta J_z$
Energy conservation	$\frac{\partial}{\partial z}\left(\rho v_z h\right)+\frac{1}{r}\frac{\partial}{\partial r}\left(\rho r v_r h\right)=\frac{\partial}{\partial z}\left(\frac{k}{C_p}\frac{\partial h}{\partial z}\right)+\frac{1}{r}\frac{\partial}{\partial r}\left(r\frac{k}{C_p}\frac{\partial h}{\partial r}\right)+\dot{S}_h$
Source term in the energy conservation equation	$\dot{S}_h=\left(\frac{J_r^2+J_z^2}{\sigma}\right)-S_r+\frac{5}{2}\frac{k_B}{e}\left(\frac{J_z}{C_p}\frac{\partial h}{\partial z}+\frac{J_r}{C_p}\frac{\partial h}{\partial r}\right)$
Combination of Ohm's law and charge conservation equation (potential approach)	$\frac{\partial}{\partial z}\left(\sigma\frac{\partial\phi}{\partial z}\right)+\frac{1}{r}\frac{\partial}{\partial r}\left(r\sigma\frac{\partial\phi}{\partial r}\right)=0$
Ohm's law (to get the radial component of current flux)	$J_r=-\sigma\frac{\partial\phi}{\partial r}$
Ohm's law (to get the axial component of current flux)	$J_z=-\sigma\frac{\partial\phi}{\partial z}$
Charge conservation equation	$\frac{\partial J_r}{\partial r}+\frac{\partial J_z}{\partial z}=0$
Faraday's law (To get the magnetic flux density)	$B_\theta=\frac{\mu_0}{r}\int_0^r J_z r dr$

Table 3 Boundary conditions (see Fig. 1 to locate every boundary)

Boundary(see Fig. 1)	(radial momentum)	(axial momentum)	(energy conservation)	(electric potential approach)
	V_r	V_z	h	ϕ
AB	0	0	$h = h_0$ (T = 3493 K) Heat flux below	$\left(\frac{\partial \phi}{\partial z}\right) = \frac{J_c}{\sigma}$ where $J_c = \frac{I}{\pi R_c^2}$
BC	0	0	$h = h_0$ (T = 3493 K)	$\left(\frac{\partial \phi}{\partial z}\right) = 0$
CD	0	$\frac{\partial}{\partial z}(\rho v_z) = 0$	$\frac{\partial h}{\partial z} = 0$	$\left(\frac{\partial \phi}{\partial z}\right) = 0$
DE	$\frac{\partial v_r}{\partial r} = 0$	$\frac{\partial v_z}{\partial r} = 0$	$\frac{\partial h}{\partial r} = 0$	$\left(\frac{\partial \phi}{\partial r}\right) = 0$
EF	0 Heat fluxes below	0	$h = h_0$ (T = 1500 K)	$\phi = 0$
AF	0	$\frac{\partial v_z}{\partial r} = 0$	$\frac{\partial h}{\partial r} = 0$	$\left(\frac{\partial \phi}{\partial r}\right) = 0$

Heat flux at the electrodes

	Heat flux mechanism	Equation
AB	Cathode fall	$Q_c = \lvert J_c \rvert V_c$ [a]
EF	Anode fall	$Q_a = \lvert J_z \rvert V_a$ [b]
EF	Convection	$Q_{conv} = \frac{0.915}{Pr_w}\left[\left(\frac{\rho_b \mu_b}{\rho_w \mu_w}\right)^{0.43}\right]\left[\rho_w \mu_w \frac{dv_r}{dr}\right]\left[h_b - h_w\right]$
EF	Radiation	$Q_{rad,i} = \int \frac{S_r}{4\pi r_{(i,j)}^2} \cos\Psi dV_j$
EF	Thomson effect	$Q_e = \frac{5J_z}{2e} k_B (\alpha T_b - T_w)$ [c]
EF	Work function	$Q_{cond} = J_z \phi_w$ [b]

[a] $V_c = 4V$ was taken from [21]

[b] $V_a + \phi_w = 6.76V$ was taken from [21]

[c] $\alpha = 1.22$ was taken from [22]

Results and Discussion

Dominance maps were produced for the nine gases analyzed, keeping the arc current and length constant at 200 A and 10 mm, respectively. In those maps, the colors indicate the major or dominant mechanism (red is radiation, light blue is conduction, green is convection, purple is the Thomson effect, and orange is Joule heating). The color bar of each mechanism corresponds to the value of power density in each cell normalized by the maximum value of that mechanism in the whole domain. The shape of the arc (visible arc) is depicted by the outer isotherm (dotted line) and the isotherm for which the conductivity is 2850 S m^{-1} is also plotted (dashed line) since in previous works, it was used to define the shape of the arc [19, 20]. Because electrical conductivity behaves differently for each gas,

Table 4 Temperature (K) corresponding to conduction and visible isotherms of all the gases simulated

Shielding gas	Conduction isotherm (dashed line)	Visible isotherm (dotted line)
Ar	10,000	7200
He	14,900	12,100
CO_2	9400	6800
O_2	10,000	7000
N_2	10,200	7600
Ar–He 50	10,500	7800
Air	9900	7100
Cl_2	9300	6200
F_2	11,200	8300

the isotherms need to be established accordingly for each map. Table 4 contains the value for both isotherms of all the gases considered in this work.

Finally, the relative importance of the dominant heat transfer mechanism is presented through isolines. For example, the isoline with a label of 0.8, means that 80% of the total heat input or output is due to the dominant heat transfer mechanism [17], and since these lines cross through several regions, the comparison can be made. We grouped the maps by the nature of the gas at standard conditions, Fig. 2 show

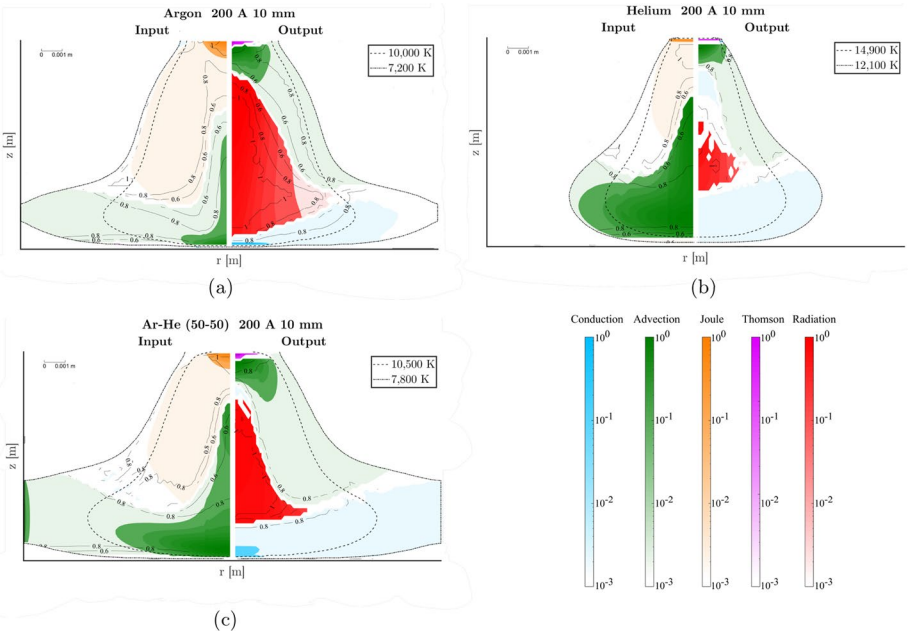

Fig. 2 Heat transfer predominance mechanism for **a** Ar, **b** He, **c** 50–50% Ar–He. Color identification: radiation = red, convection = green, conduction = light blue, Thomson = purple, Joule heating = orange. In each case, the edge of the arc (arc shape) is presented along with the relative importance of the dominant heat transfer mechanisms through isolines (Color figure online)

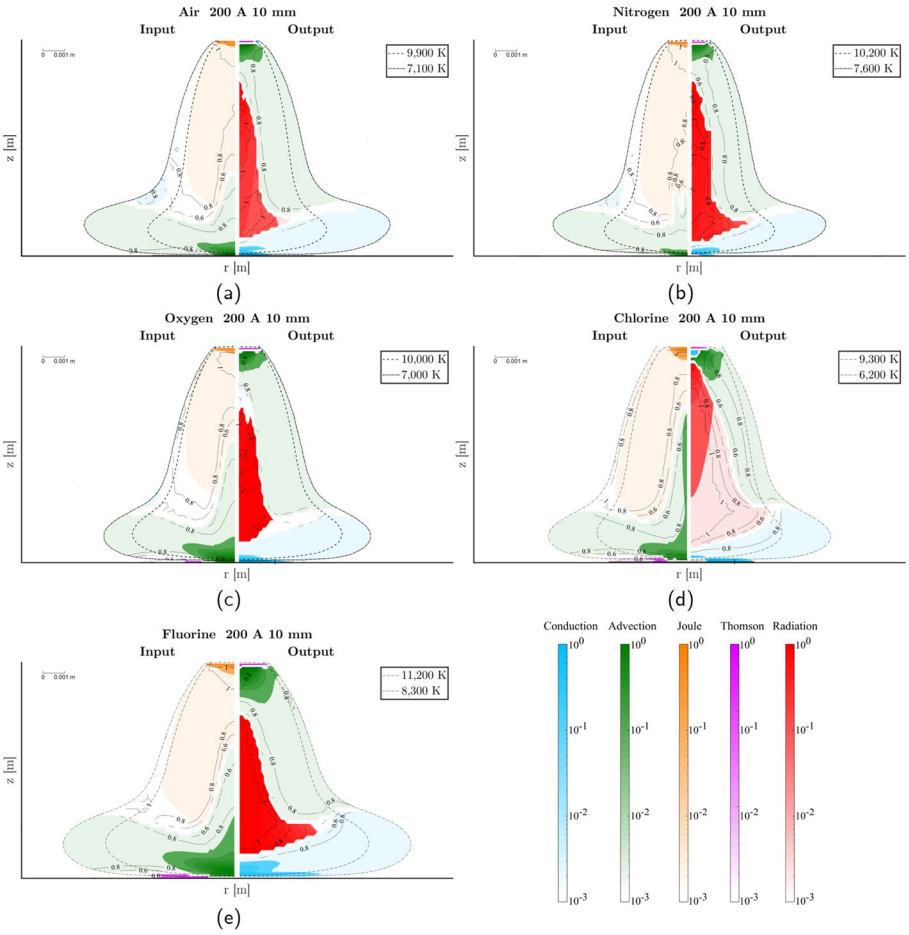

Fig. 3 Heat transfer predominance mechanism for **a** air, **b** N_2, **c** O_2, **d** Cl_2, **e** F_2. Color identification: radiation = red, convection = green, conduction = light blue, Thomson = purple, Joule heating = orange. In each case, the edge of the arc (arc shape) is presented along with the relative importance of the dominant heat transfer mechanisms through isolines (Color figure online)

monoatomic gases such as Ar, He, and Ar–He mixtures, Fig. 3 shows diatomic gases such as N_2, O_2, F_2, Cl_2, and air; and finally, the only triatomic gas, CO_2, is displayed in Fig. 4. The maps come in two parts, bisected by the axis of symmetry: the left-hand side corresponds to energy inputs and the right-hand side shows the outputs. Regardless of the type of gas, the mechanisms for the input and output of energy are similar. The inputs, from the cathode to the anode, are Joule heating and convection, while the outputs, from the cathode to the anode, are the Thomson effect, convection, radiation and conduction. What changes in the maps is the area over which each major mechanism dominates and its intensity.

Analyzing the differences in the mechanisms from the largest to the minor areas for each color (mechanism) has to consider the physical properties of every gas and the arc

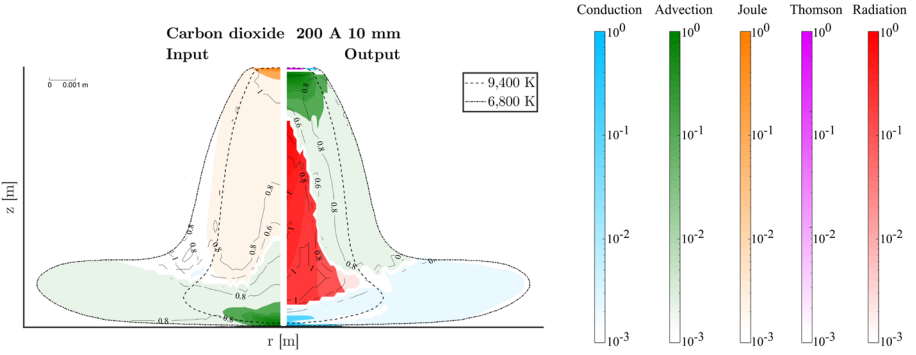

Fig. 4 Heat transfer predominance mechanism for CO_2. Color identification: radiation = red, convection = green, conduction = light blue, Thomson = purple, Joule heating = orange. In each case, the edge of the arc (arc shape) is presented along with the relative importance of the dominant heat transfer mechanisms through isolines (Color figure online)

characteristics that determine the magnitude of the heat transfer mechanism. The most relevant mechanisms are discussed below.

Summary of Results

Table 5 presents a summary of some basic characteristics of each gas. The maximum temperature and velocity in the arc are provided. Most of the arcs have maximum temperatures of 20,000 to 23,000 K. Air, O_2 and N_2 have the highest velocities, followed by He and CO_2. Other parameters such as the arc column voltage, and those related to the interactions of the arc and the weld pool, the total heat flow to the weld pool, maximum pressure and maximum shear stress, are also presented. He, N_2, air and CO_2 exhibit the highest arc voltages and since arc current is constant, it is concluded that these gases have the highest average Ohmic resistances of those studied. A consequence of high Ohmic resistance is that these

Table 5 Characteristic values of the arc and its interaction with the weld-pool for the shielding gases studied in this work

Shielding gas	T_{max} (K)	V_{max} (m s^{-1})	V_{LTE} (V)	Heat flow at the anode (W)	Maximum pressure at the anode (Pa)	Maximum shear stress at the anode (Pa)
Ar–He 50%	2.11×10^4	2.84×10^2	14.1	1.55×10^3	2.84×10^2	4.75×10^1
CO_2	2.15×10^4	6.06×10^2	22.0	2.39×10^3	1.03×10^3	1.49×10^2
F_2	2.07×10^4	4.68×10^2	16.7	1.78×10^3	5.92×10^2	9.65×10^1
N_2	2.40×10^4	9.63×10^2	25.0	2.58×10^3	2.26×10^3	2.24×10^2
Air	2.02×10^4	7.21×10^2	23.0	2.37×10^3	1.60×10^3	2.20×10^2
He	2.09×10^4	8.36×10^2	26.0	2.71×10^3	2.56×10^2	4.73×10^1
Ar	2.13×10^4	3.10×10^2	14.4	1.46×10^3	6.01×10^2	4.07×10^1
O_2	2.00×10^4	6.29×10^2	19.0	1.64×10^3	8.03×10^2	9.60×10^1
Cl_2	1.81×10^4	2.02×10^2	13.6	6.91×10^2	1.61×10^2	1.42×10^1

gases deliver more heat to the anode than the other gases, indicating the Joule heat's importance in the heat transferred from the arc to the weld pool. It is difficult to conclusively establish the best gas for heating since we kept the arc length and arc current unchanged but the results presented give guidance for a better shielding gas selection.

Finally, the gases that apply most pressure and shear stress to the weld pool are N_2, air, and CO_2, while the gases causing lowest shear are Cl_2, He, F_2 and Ar, i.e., the former gases are more likely to perturb the weld pool than the latter gases. This magnitude of the pressure and shear stress is correlated to the vertical extent of the region of Joule heating dominance. When Joule heating dominance extends to close to the workpiece, this indicates that the arc remains constricted, increasing pressure and shear stress.

Joule Effect

The Joule effect is the main heating mechanism near the cathode. He and Ar are two extreme cases; Ar has the largest Joule zone and intensity while He has the least extensive and intense Joule contribution. Helium has two important properties that distinguish it from the other gases. Both arise from its high ionization energy. First, the electrical conductivity of He is lower than the other gases up to about 20,000 K as can be seen in Fig. 5a and the viscosity is higher above 10,000 K as can be seen in Fig. 5b. The low electrical conductivity of helium means that the region conducting electricity is relatively narrow near the cathode compared to the argon arc, which means that the Joule heating region is smaller in He than in Ar. The high viscosity implies that the flow spreads radially at a relatively low axial position (i.e. closer to the cathode). The two effects combine to give a relatively small region of Joule heating dominance and a correspondingly large region of convective heat transfer dominance as it will be seen in the next section.

Near the cathode, the arc's most elevated temperatures and the highest current densities are present. Since the arc operates at the same current, it is clear that the Joule effect comes from the electric resistance (inversely proportional to the electric conductivity) and consequently, Ar presents more electric resistance than He in this region.

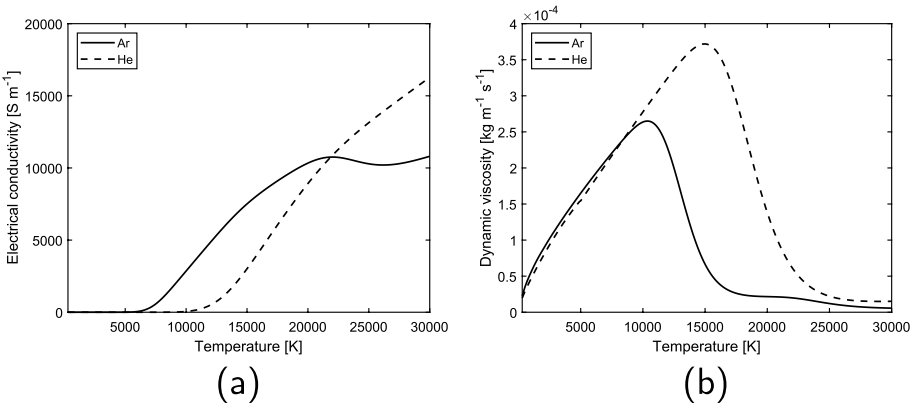

Fig. 5 Thermophysical properties of Ar and He as a function of temperature, **a** electrical conductivity, **b** dynamic viscosity

Convection Near the Anode

The other major source of positive energy in the arc is the convection, which dominates near the anode as an input. The convective heat transfer is computed as the product ρVh. Therefore, it can be stated that the arc produces heat by the Joule effect near the cathode and delivers heat to the workpiece by convection. In this case, the extreme cases are He (highest delivery by convection) and N_2 (lowest convection dominance zone). Figure 6 shows the velocity profiles and enthalpy contours of the two gases since the convective heat transfer depends directly on the velocity and enthalpy. Although the N_2 plasma jet velocity is greater than the helium arc velocity near the anode, the region inside the He enthalpy contour of value 2.9×10^7 J is significantly larger than that inside the corresponding N_2 enthalpy contour, so the convection dominance zone is larger in the He map. Besides, as stated in the previous section, the high viscosity of helium at temperatures greater than 10,000 K means that the region over which the convective flow is important is larger in He than in other gases. The helium viscosity can be seen in Fig. 5b.

Radiation

Radiation is the primary energy output mechanism in the arc column. Figure 7 shows the net emission coefficient for the two extreme cases of Ar (highest radiation intensity and extent) and He (lowest intensity and extent). Ar emits radiation several orders of magnitude more strongly than He at a given temperature, which explains the difference.

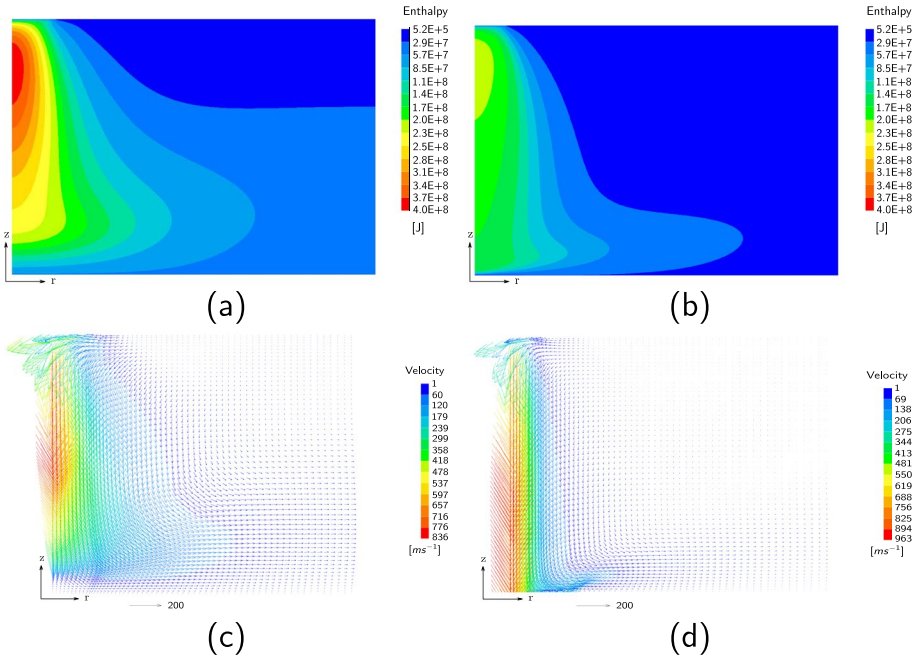

Fig. 6 Enthalpy contours for He (**a**) and N_2 (**b**). Velocity profile for He (**c**) and N_2 (**d**)

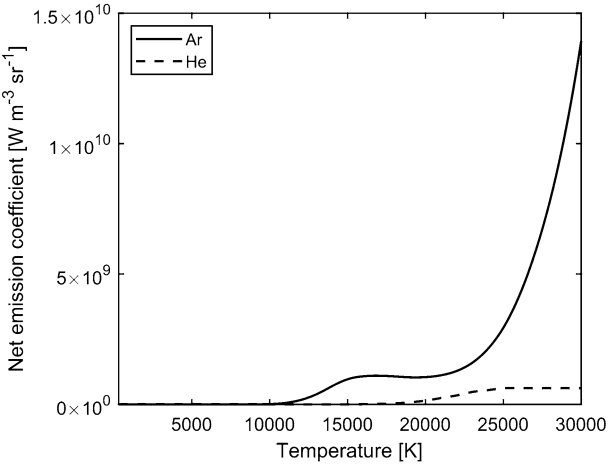

Fig. 7 Net emission coefficient for Ar and He as a function of temperature

Conduction

The output by heat conduction near the anode counterbalances the convection delivered in the boundary layer zone, which is produced by the impingement of the plasma jet and subsequent radial deflection. Helium and fluorine are the extreme cases, with He having the lowest and F_2 the highest heat losses by conduction. This mechanism is explained by conductive heat flux to the workpiece, which has a much lower temperature than the plasma. The temperature gradient near the anode is much greater (one order of magnitude) in F_2 than in He, as shown in Fig. 8a and b. Another important factor is the thermal conductivity at low temperatures, which, for molecular gases such as F_2, has peaks in the temperature range close to the workpiece. The peaks arise from molecular dissociation reactions, as can be seen in Fig. 8c.

Conclusions

The electric arcs formed at atmospheric pressure from nine gases have been explored through numerical simulation. The gases are monoatomic (Ar, He, 50% Ar–50% He), diatomic (air, N_2, O_2, F_2, Cl_2), and triatomic (CO_2). The parameters used for all simulations were 200 A and 10 mm arc length.

The simulations indicate that for all gases, the dominant heat transfer mechanisms are the same in comparable regions of the arc; however, the relative size of the regions of dominance varies with the properties of the gases in a predictable way.

The Joule effect is the dominant heat input mechanism near the cathode, and has the largest area of dominance in Ar, and smallest in He. Convection is the dominant heat input mechanism near the anode, with the largest area of dominance in He, and smallest in N_2. Radiation is the primary energy output in the arc column, and has the largest area of dominance in Ar, and smallest in He. The magnitude of radiated power in Ar is several orders of magnitude greater than He.

Conduction is the dominant energy output from the arc near the anode, consistent with the heat transfer through a boundary layer to the surface of the workpiece. The highest

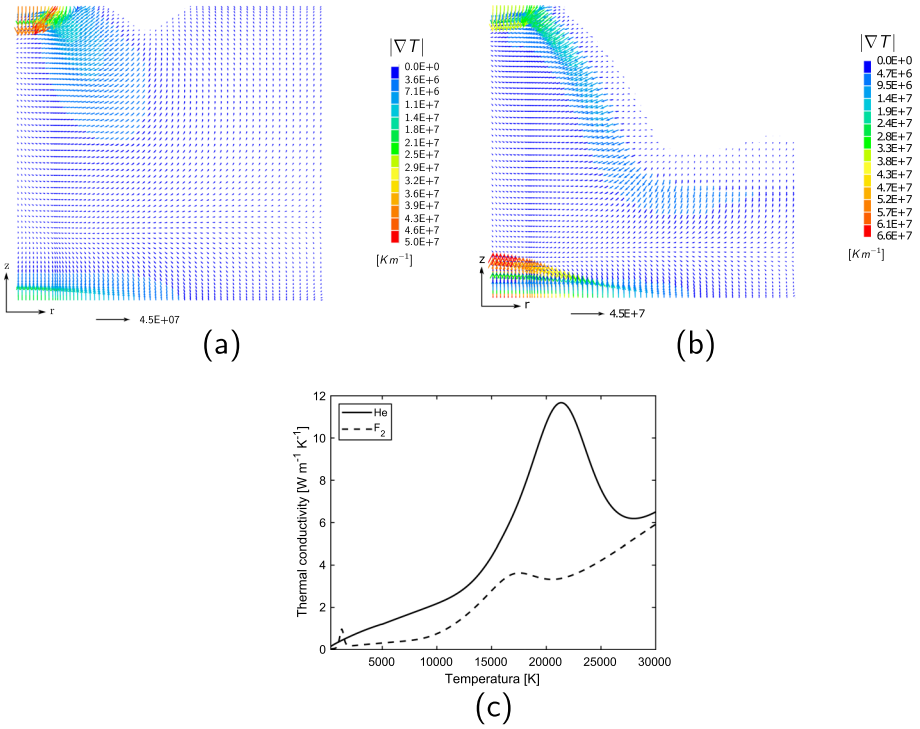

Fig. 8 Temperature gradient vector plot for He (**a**) and F_2 (**b**), thermal conductivity for He and F_2 (**c**)

conduction rate is observed for F_2, consistently with its highest thermal gradient and the lowest for He. Molecular gases tend to have higher conduction rates.

Although further considerations are needed (e.g. deterioration or melting and evaporation of the electrode) before applying the results to welding applications, the present work helps to understand the physical mechanisms of heat transfer present in the arc, and giving a foundation to analyze the effect of novel arc gas compositions.

Appendix 1: Calculation of Thermophysical Properties

The thermophysical properties of the plasmas were obtained using standard methods under the assumption of LTE. The composition of the plasma was calculated as a function of temperature by the method of Gibbs free energy minimization. The thermodynamic properties (density, specific heat, enthalpy) were then obtained from the composition and the thermodynamic properties of each species present. The transport coefficients (viscosity, thermal conductivity, electrical conductivity) were calculated using the Chapman–Enskog method [28]. More detailed descriptions of the methods used have been given previously [24–26, 29, 30].

The species considered and sources of the collision integrals have been given for argon [24, 30], helium and argon–helium [26], nitrogen [25, 29], and oxygen and carbon dioxide [25] plasmas. Note that the C–C collision integrals used in the calculation of carbon dioxide plasma properties have been updated to those given by Stallcop et al. [31].

The equivalent data have not been published for fluorine and chlorine plasmas and are presented here.

The chlorine species considered were Cl_2, Cl, Cl^-, Cl^+, Cl^{2+}, Cl^{3+} and Cl^{4+}. The thermodynamic properties of the atoms and positive ions were calculated from the electronic energy levels in the NIST database [32]. The thermodynamic properties for Cl_2 and Cl^- were taken from the JANAF tables [33].

The fluorine species considered were F_2, F, F^-, F^+, F^{2+} and F^{3+}. The thermodynamic properties of the atoms and positive ions were calculated from the electronic energy levels given by Moore [34]. The thermodynamic properties for F_2 and F^- were taken from the JANAF tables [33].

The Cl_2–Cl_2, F_2–F_2, Cl–Cl and F–F collision integrals, and the Cl–Cl^+ and F–F^+ elastic interaction cross-section, were calculated using the phenomenological potential [35]. The data required to calculate the potential are given in Table 6; the effective electron number was calculated using the expression recommended by Cambi et al. [36]. The charge-exchange cross sections for the Cl–Cl^+ and F–F^+ interactions were obtained from the data of Sakabe and Izawa [37]. The Cl–Cl^+ and F–F^+ collision interactions were obtained from the charge-exchange and elastic cross-sections using standard methods [24].

Calculation of electron-neutral collision integrals requires momentum transfer cross-section data [24]. For e-Cl_2, these were taken from Rescigno [40], while the data for e-Cl were taken from Saha [41], following the recommendation of Christophorou and Oltoff [42]. For e-F, the momentum transfer cross-section data of Robinson and Geltman [43] were used, while for e-F_2, the total elastic cross-section data of Schneider and Hay [44] were adopted.

The net emission coefficients of Ar, O_2, C, Cl_2 and F_2 were calculated using the method of Cram [45]. Those for He were taken from Cressault et al.[46] and for N_2 from Ernst et al. [47]. For CO_2, air and Ar–He, a mole-fraction-weighted average of the constituent atoms was used. In all cases, an absorption length R_p of 1 mm was selected. Note that Ernst et al. did not provide data for $R_p = 1$ mm, so their $R_p = 3$ mm data was multiplied by a factor of 1.5 to account for the decreased absorption. The choice of R_p is in accordance with the advice of Cressault et al. [48], who recommended a value corresponding to the radius at which the arc temperature has fallen to about 80% of its value on axis, but noted that the choice was not critical. For the Ar and He arcs, whose temperature profiles are shown in Refs. [17] and [20] respectively, the radii at which the temperature falls to 80% of its maximum value are about 0.8 and 1.3 mm, respectively. Given the uncertainties noted by Cressault et al. [48], $R_p = 1$ mm is a reasonable approximation.

Table 6 Data required for calculation of phenomenological potential

Species	Polarization (10^{-20} m^{-3})	Ground state spin multiplicity	Effective electron number
Cl_2	4.61 [38]	1	1
Cl	2.18 [38]	2	7.727
Cl^+	1.23 [39]	3	–
F_2	1.259 [35]	1	1
F	0.557 [38]	2	6.2
F^+	0.272 [35]	3	–

Appendix 2: List of Symbols

Magnitude	Description	Units
B_θ	Azimuthal magnetic flux density	(Tesla)
b	Subscript indicating property at the edge of the momentum boundary layer	
C_p	Specific heat	(J kg^{-1} K^{-1})
dV_j	Volume element in the arc region	(m^3)
e	Electron charge $1.602176634\ 10^{-19}$	(C)
h	Enthalpy	(J kg^{-1})
I	Current	(A)
J_r	Radial current density component	(A m^{-2})
J_z	Axial current density component	(A m^{-2})
J_c	Cathode current flux density	(A m^{-2})
k	Thermal conductivity	(W m^{-1} K^{-1})
k_B	Boltzmann's constant 1.380649×10^{-23}	(m^2 kg s^{-2} K^{-1})
P	Pressure	(N m^{-2})
Pr_w	Prandtl number	(–)
Q_a	Heat flux by anode fall	(W m^{-2})
Q_c	Heat flux by cathode fall	(W m^{-2})
Q_cond	Heat flux by condensation of electrons	(W m^{-2})
Q_conv	Convective heat flux	(W m^{-2})
Q_e	Heat flux by Thomson effect	(W m^{-2})
$Q_\mathrm{rad,i}$	Heat flux by radiation	(W m^{-2})
r	Radial coordinate	(m)
$r_\mathrm{i,j}$	Vector linking each surface element at the anode to each volume element in the arc	(m)
R_c	Cathode spotradius	(m)
$\dot{S}_\mathrm{h}$	Source term in the energy conservation equation	(W m^{-3})
S_r	Net radiative emission coefficient	(W m^{-3})
T	Temperature	(K)
V_c	Cathode fall	(V)
v_r	Radial velocity	(m s^{-1})
v_z	Axial velocity	(m s^{-1})
w	Subscript indicating property at the anode surface	
z	Axial coordinate	(m)
V_LTE	Voltage fall along the centerline in the LTE part of the column	(V)
Greek		
α	Ratio of electron temperature and plasma temperature at anode fall	(–)
μ	viscosity	(kg m^{-1} s^{-1})
μ_0	Vacuum magnetic permeability $1.25663706212 \times 10^{-6}$	(H m^{-1})
ρ	Plasma density	(kg m^{-3})
σ	Electric conductivity	(S m^{-1})
ϕ	Electric potential	(V)
ϕ_w	Work function of the workpiece	(V)

Magnitude	Description	Units
Ψ	Solid angle between $r_{i,j}$ and the vector normal to the anode surface	(sr)

Acknowledgements Rodrigo Villarreal Medina is a Ph D student in the "Programa de Doctorado en Ingeniería Química", at the Universidad Nacional Autónoma de México (UNAM). He thanks CONACYT for receiving a doctoral fellowship (Grant Number CVU 1002868).

Open Access This article is licensed under a Creative Commons Attribution 4.0 International License, which permits use, sharing, adaptation, distribution and reproduction in any medium or format, as long as you give appropriate credit to the original author(s) and the source, provide a link to the Creative Commons licence, and indicate if changes were made. The images or other third party material in this article are included in the article's Creative Commons licence, unless indicated otherwise in a credit line to the material. If material is not included in the article's Creative Commons licence and your intended use is not permitted by statutory regulation or exceeds the permitted use, you will need to obtain permission directly from the copyright holder. To view a copy of this licence, visit http://creativecommons.org/licenses/by/4.0/.

References

1. Lancaster JF (1999) Metallurgy of welding. William Andrew Publishing, Norwich
2. Murphy AB, Lowke JJ (2017) Heat transfer in arc welding. Springer, Cham, pp 1–72
3. Murphy AB (2015) A perspective on arc welding research: the importance of the arc, unresolved questions and future directions. Plasma Chem Plasma Process 35:471–489
4. Tanaka M (2004) An introduction to physical phenomena in arc welding processes. Weld Int 18(11):845–851
5. Tanaka Y, Fujino T, Iwao T (2019) Review of thermal plasma simulation technique. IEEJ Trans Electr Electron Eng 14(11):1582–1594
6. Uhrlandt D (2016) Diagnostics of metal inert gas and metal active gas welding processes. J Phys D Appl Phys 49:313001
7. Shigeta M, Tanaka M (2019) Visualization of electromagnetic-thermal-fluid phenomena in arc welding. Jpn J Appl Phys 59:SA0805
8. Suzuki R, Matsuoka Y, Hirotani D, Nezu A, Mori S, Akatsuka H (2021) Spectroscopic measurement of arc-discharge argon plasma plume injected into water. IEEJ Trans Electr Electron Eng 16:364–373
9. Pan J, Yang L, Hu S, Chen S (2017) Numerical analysis of keyhole formation and collapse in variable polarity plasma arc welding. Int J Heat Mass Transf 109:1218–1228
10. Liu Y, Wang X, Zhong L, Yang A, Rong M, Wu J (2018) Influence of Al, Fe or Cu vapour on thermophysical properties of CO_2 plasmas. Eur Phys J D 72(12):1–12
11. Singh B, Singhal P, Saxena KK (2019) Investigation of thermal efficiency and depth of penetration during GTAW process. Mater Today Proc 18:2962–2969
12. Pichot F, Danis M, Lacoste E, Danis Y (2013) Numerical definition of an equivalent GTAW heat source. J Mater Process Technol 213(7):1241–1248
13. Ai Y, Jiang P, Shao X, Li P, Wang C (2017) A three-dimensional numerical simulation model for weld characteristics analysis in fiber laser keyhole welding. Int J Heat Mass Transf 108:614–626
14. Traidia A, Roger F, Chidley A, Schroeder J, Marlaud T (2011) Effect of helium–argon mixtures on the heat transfer and fluid flow in gas tungsten arc welding. World Acad Sci Eng Technol Int J Mech Aerosp Ind Mechatron Manuf Eng 5:223–228
15. Lu F, Wang HP, Murphy AB, Carlson BE (2014) Analysis of energy flow in gas metal arc welding processes through self-consistent three-dimensional process simulation. Int J Heat Mass Transf 68:215–223
16. Schnick M, Fussel U, Hertel M, Rose S, Haessler M, Spille-Kohoff A, Murphy AB (2011) Numerical investigations of the influence of metal vapour in GMA welding. Weld World 55:114–120
17. Velazquez-Sanchez A, Delgado-Alvarez A, Mendez P, Murphy A, Ramirez-Argaez M (2021) Dominant heat transfer mechanisms in the GTAW plasma arc column. Plasma Chem Plasma Process 41:09
18. Ramirez MA, Trapaga G, McKelliget J (2003) A comparison between two different numerical formulations of welding arc simulation. Model Simul Mater Sci Eng 11:675–695
19. Delgado-Alvarez A, Mendez PF, Ramirez-Argaez MA (2019) Dimensionless representation of the column characteristics and weld pool interactions for a DC argon arc. Sci Technol Weld Join 24:634–643

20. Delgado-Alvarez A, Mendez PF, Murphy AB, Ramirez-Argaez MA (2021) Generalized representation of arc shape, arc column characteristics and arc-weld pool interactions for dc electric arcs burning in monoatomic gases. J Phys D Appl Phys 54:055001
21. McKelliget J, Szekely J (1986) Heat transfer and fluid flow in the welding arc. Metall Trans A 17:1139–1148
22. Ushio M, Szekely J, Chang CW (1981) Mathematical modelling of flow field and heat transfer in high-current arc discharge. Ironmak Steelmak 8(76):279–286
23. Murphy AB (2001) Thermal plasmas in gas mixtures. J Phys D Appl Phys 34:R151–R173
24. Murphy AB, Arundell CJ (1994) Transport coefficients of argon, nitrogen, oxygen, argon–nitrogen, and argon–oxygen plasmas. Plasma Chem Plasma Process 14:451–490
25. Murphy AB (1995) Transport coefficients of air, argon–air, nitrogen–air, and oxygen–air plasmas. Plasma Chem Plasma Process 15:279–307
26. Murphy AB (1997) Transport coefficients of helium and argon–helium plasmas. IEEE Trans Plasma Sci 25:814–890
27. Ramirez MA, Trapaga G, McKelliget J (2004) A comparison between different numerical formulations for welding arc representations. J Mater Process Technol 155–156:1634–1640 (**Proceedings of the International Conference on Advances in Materials and Processing Technologies: Part 2**)
28. Hirschfelder J, Curtiss C, Bird R (1954) Molecular theory of gases and liquids. Wiley, New York
29. Murphy AB (2012) Transport coefficients of plasmas in mixtures of nitrogen and hydrogen. Chem Phys 398(1):64–72
30. Murphy AB, Tam E (2014) Thermodynamic properties and transport coefficients of arc lamp plasmas: argon, krypton and xenon. J Phys D Appl Phys 47(29):295202
31. Stallcop JR, Partridge H, Pradhan A, Levin E (2000) Potential energies and collision integrals for interactions of carbon and nitrogen atoms. J Thermophys Heat Transf 14(4):480–488
32. Kramida A, Ralchenko Y, Reader J, NIST ASD Team (2020) NIST atomic spectra database (version 5.8). National Institute of Standards and Technology, Gaithersburg
33. Chase MW (1998) NIST-JANAF thermochemical tables, 4th edn. Monograph 9 of Journal of physical and chemical reference data. American Chemical Society, Washington
34. Moore C (1949) Atomic energy levels, vol 1. National Bureau of Standards, Washington, DC
35. Wang X, Zhong Z, Cressault Y, Gleizes A, Rong M (2014) Thermophysical properties of SF6-Cu mixtures at temperatures of 300–30,000 K and pressures of 0.01–1.0 MPa: part 2. Collision integrals and transport coefficients. J Phys D Appl Phys 47(49):495201
36. Cambi R, Cappelletti D, Liuti G, Pirani F (1991) Generalized correlations in terms of polarizability for van der Waals interaction potential parameter calculations. J Chem Phys 95(3):1852–1861
37. Sakabe S, Izawa Y (1991) Cross sections for resonant charge transfer between atoms and their positive ions: collision velocity ≤ 1 a.u. At Data Nucl Data Tables 49(2):257–314
38. Lide D (2003) Handbook of chemistry and physics, vol 84. CRC Press, Boca Raton
39. Medved M, Fowler P, Hutson J (2000) Anisotropic dipole polarizabilities and quadrupole moments of open-shell atoms and ions: O, F, S, Cl, Se, Br and isoelectronic systems. Mol Phys 98(7):453–463
40. Rescigno T (1994) Low-energy electron–collision processes in molecular chlorine. Phys Rev A 50(2):1382–1389
41. Saha H (1996) Ab initio calculation for low-energy elastic scattering of electrons from chlorine atoms. Phys Rev A 53(3):1553–1558
42. Christophorou L, Olthoff J (1999) Electron interactions with Cl_2. J Phys Chem Ref Data 28(1):131–169
43. Robinson EJ, Geltman S (1967) Single- and double-quantum photo detachment of negative ions. Phys Rev 153(1):4–8
44. Schneider B, Hay P (1976) Elastic scattering of electrons from F2: an R-matrix calculation. Phys Rev A 13(6):2049–2056
45. Cram LE (1985) Statistical evaluation of radiative power losses from thermal plasmas due to spectral lines. J Phys D Appl Phys 18:401–411
46. Cressault Y, Rouffet ME, Gleizes A, Meillot E (2010) Net emission of Ar, H_2, He thermal plasmas at atmospheric pressure. J Phys D Appl Phys 43:335204
47. Ernst KA, Kopainsky JG, Maecker HH (1973) The energy transport, including emission and absorption, in N_2-arcs of different radii. IEEE Trans Plasma Sci 1(4):3–16
48. Cressault Y, Gleizes A, Riquel G (2012) Properties of air–aluminum thermal plasmas. J Phys D Appl Phys 45:265202

Publisher's Note Springer Nature remains neutral with regard to jurisdictional claims in published maps and institutional affiliations.